Mg-doped $CuFeO_2$ Photocathodes for Photoelectrochemical Reduction of Carbon Dioxide

*Jing Gu, Anna Wuttig, Jason W. Krizan, Yuan Hu, Zachary M. Detweiler, Robert J. Cava, and Andrew B. Bocarsly**

**Department of Chemistry, Princeton University, Princeton, New Jersey, 08544, United States*

[Email]: bocarsly@princeton.edu

RECEIVED DATE

Keywords

Doped $CuFeO_2$, oxide photoelectrode, photoelectrochemical CO_2 reduction, electrochemical band characterization

Abstract

Mg-doped $CuFeO_2$ delafossite is reported to be photoelectrochemically active for CO_2 reduction. The material was prepared via conventional solid-state methods, and subsequently assembled into an electrode as a pressed pellet. Addition of a Mg^{2+} dopant is found to substantially improve theconductivity of the material, with 0.05 % Mg-doped $CuFeO_2$ electrodes displaying photocathodic currents under visible irradiation. Photocurrent is found to onset at irradiation wavelengths ~800 nm with the incident-photon-to-current efficiency (IPCE) reaching a value of 14 % at 340 nm using an applied electrode potential of -0.4 V *vs.* saturated calomel electrode (SCE). Photoelectrodes were determined to have a -1.1 V *vs.* SCE conduction band edge, and were found capable of the reduction of CO_2 to formate at 400 mV of underpotential. The conversion efficiency maximized at -0.9 V *vs.* SCE, with H_2 production contributing to considerable faradaic efficiency loss. These results highlight the potential to produce Mg-doped p-type metal oxide photocathodes with band structure tuned to optimize CO_2 reduction.

Introduction

Recycling of carbon dioxide via photoconversion to fuels is a challenging, yet promising avenue for achieving a sustainable alternative to conventional fossil fuels. Use of photon energy to reduce CO_2 requires materials that efficiently interact with light to yield high-energy photogenerated electrons. Various systems yielding photoreduced CO_2 products have been reported, including molecular photocatalysts,[1] molecular catalysts with photosenitizers,[2,3] nanoscale semiconductor materials,[4-6] and photoelectrodes.[7,8] For producing value-added multiple-electron reduced products of CO_2, semiconductor photoelectrodes are of interest because they have shown high yields of methanol and formaldehyde. [9,10]

At a semiconductor/electrolyte interface photogenerated minority charges are driven into the electrolyte by the resultant electric field. These charges can perform redox reactions, such as direct CO_2 reduction when a p-type semiconductor is used as the electrode. Although p-type III-V semiconductor electrodes have been demonstrated to yield high CO_2 reduction faradaic efficiencies,[4] these materials are relatively unstable under illumination in an aqueous electrochemical environment, and further suffer from excessively high overpotentials.[7,11] Therefore, a more stable and affordable semiconductor material with a band gap suitable for conversion of insolation is desired.

Recent studies on metal-oxide-based electrodes report relatively enhanced thermodynamic stability and use of earth abundant materials, thereby suggesting that these materials may be much improved candidates as photoelectrodes.[12] Many well-known oxide photoelectrodes have been formed into n-type photoanodes,[13,14] but, are not suitable for the desired photoactive CO_2 reduction reaction, for which p-type electrodes (photocathodes) are

required. While non-oxide-based p-type semiconductors have been evaluated under visible light conditions for CO_2 reduction,[15-17] oxide-based p-type photoelectrodes have received little attention in this regard. Thus, it is desirable to find alternative oxide-based p-type semiconductor electrodes for solar-driven CO_2 conversion processes.

Recently, a p-type $CaFe_2O_4$ photoelectrode was reported to produce hydrogen from water.[12] In the $CaFe_2O_4$ system, it has been proposed that the semiconductor valence band (VB) primarily has oxygen 2p character, and that the conduction band (CB) is dominated by iron 3d states.[18] The Fe 3d-dominated conduction band (CB) edge of the material, -0.9 V vs. saturated calomel electrode (SCE), hovers at a potential more negative than the redox potential of CO_2. Therefore, photogenerated electrons in this system are thermodynamically capable of reducing CO_2. Based on this example it appears that oxides with Fe 3d-dominated CB states are promising candidate photoelectrodes for CO_2 reduction. To allow for maximum photon absorption, however, a narrower band gap material than $CaFe_2O_4$, ($E_g \sim 1.9$ eV), is desired. Compared with large band gap oxide semiconductors, which have VBs dominated by oxygen anion 2p states and CBs dominated by transition metal cation 4s or 3d states, VBs consisting of copper $3d^{10}$ states have been calculated to result in a higher energy valence band edge and therefore a smaller band gap.[19] To this end, copper (I) delafossite compounds ($CuMO_2$, where M is a trivalent transition metal cation) are of interest. Furthermore, optical excitation of $CuMO_2$ primarily involves a metal to metal transition, between the Cu-d^{10} and M-d states, which theoretically protects the metal-oxide bonds increasing compound stability.[20]

The crystal structure of $CuMO_2$ consists of planes of edge-sharing M (III) O_6 octahedra separated by layers of O-Cu (I)-O sticks. [21,22] Doping of the trivalent metal site in the delafossite structure with a divalent metal has been well known to increase the conductivity. However, it has

not yet been determined why this conductivity trend is observed. [23]Mg doping is expected to contribute holes if it substitutes for M (III) or it replaces three Cu (I) in the intermediary layers. The defect chemistry of defect chemistry of delafossites has not been previously established.

Here we report a new way to incorporate and utilize Mg-doped $CuFeO_2$ into a photoelectrochemical cell for CO_2 reduction. We choose $CuFeO_2$ as the host material due to its small band gap for visible light absorption and anticipated interfacial energetics, which are expected to be well matched to the CO_2 reduction energy levels.[24] Unlike prior materials in this class that have been evaluated as semiconductor electrodes, the material reported here is doped with Mg to increase conductivity, facilitating the p-type behavior required for use as a photocathode for reduction reactions.[25,26] In contrast to the previous report involving electrodeposition of a $CuFeO_2$ electrode material,[27] the $CuFeO_2$ material employed here was prepared by high temperature solid-state synthesis, and its back-side contact was improved using a sputtered Au layer to generate an ohmic interface. In addition to examining the electrodes photophysical properties, we also report the photoelectrochemical CO_2 reducing capabilities of these Mg-doped $CuFeO_2$ electrodes.

Experimental Methods

Materials. Sodium hydroxide (99 %, Fisher), sodium bicarbonate (≥ 99 %, Fisher), argon (99.8 %, Airgas), carbon dioxide (99.8 %, Airgas), deuterium oxide (99.9 %, Cambridge Isotope Laboratories Inc.), CuO (99.7 %, Alfa Aesar), Fe_2O_3 (99.99 %, Alfa Aesar), and MgO (99.9 %, Alfa Aesar) were used without further modification.

Sample and Electrode Preparation. High purity $CuFe_{1-x}Mg_xO_2$ (x=0.0005, 10^{19} cm^{-3} majority carriers based on the reported unit cell volume) [28] powder was prepared by grinding

stoichiometric amounts of the precursors - CuO, Fe_2O_3, and MgO. The oxide mixture was fired in a covered alumina crucible at 850 °C under a flowing argon atmosphere for 96 hours, with one intermediate grinding, after which it was pressed into a pellet (0.5 – 1 mm thickness, 0.785 cm^2 area) and annealed at 850 °C for 12 hours. Solid state reaction progress was monitored by powder X-ray diffraction (XRD) on a Rigaku Miniflex II. Diffraction experiments evaluating the surface layer of the electrodes (before and after the photoelectrochemical experiments) were carried out on a Bruker D8 Focus X-Ray Diffractormeter. Both diffractometers use a Cu *K*α X-ray source and a graphite diffracted beam monochromator.

Ohmic contacts were made and tested by sputtering gold layers (~100 nm thick) onto opposing sides of the sample and attaching copper wires (Angstrom Metal Sputter). The linear current-voltage curve (Figure 1 inset), obtained by performing a potential sweep experiment with this configuration indicated the formation of ohmic contacts. For use in solution, the back-side of a pellet of p-$CuFeO_2$ was gold sputtered and connected to an external copper wire with conducting silver epoxy (Epoxy Technology H31). The assembly was covered with a glass tube and sealed with insulating epoxy cement (Loctite 0151 Hysol).

Photoresponse Characterization. UV-Vis-NIR spectra were collected using a Horiba Lab Ram Aramis Spectrometer (light source: Newport 66353) in reflection mode. Sample absorption was determined using the acquired reflectance spectrum and assuming that optical transmission was negligible.[29] To determine photocurrent density, linear sweep voltammetry experiments under chopped light were performed using a PTI 75W Xe source with a pyrex UV cut off filter. This source provides broadband illumination from 350 nm to 1350 nm with an intensity of 890 mW/cm^2 to the electrode surface. All photoresponse measurements (open circuit voltage and incident-photon-to-current efficiency (IPCE) measurements) were performed in a custom-

fabricated three neck round bottom reactor with quartz windows. Mg-doped $CuFeO_2$ was used as the working electrode, Pt mesh (Sigma Aldrich) as the counter electrode, and a standard calomel electrode (SCE, Accument) as the reference electrode in 0.1 M $NaHCO_3$ aqueous electrolyte. For IPCE measurements, 10 nm-band pass filters, centered at 340 nm, 490 nm, 638 nm, 700 nm and 780 nm were used. Photocurrent density at each irradiation intensity (ΔJ_λ) was monitored by finding the difference in dark and photocurrent densities at a given applied voltage bias. (See for example, Figure S1, which provides the photocurrent density for 490 nm irradiation using an electrode held at -0.4 V *vs.* SCE.) The total photon flux (I) was measured at each wavelength by a Si photodiode (Fieldmaster 33-0506, Coherent Inc.), placed at a distance equivalent to that of the working electrode. The incident-photon-to-current conversion efficiency (IPCE %) for monochromatic light was calculated using Equation 1.

$$IPCE\% = \frac{1240 \times \Delta J_\lambda \left(\frac{mA}{cm^2}\right)}{\lambda(nm) \times I\left(\frac{mW}{cm^2}\right)} \times 100 \qquad (1)$$

The photon flux incident on the semiconductor was corrected for the absorbance of the pyrex reactor and the aqueous electrolyte (Table S1 and Figure 2). Each data point for the IPCE experiment was measured four times, which is considered in the reported experimental error values.

Band Characterization. Open circuit photovoltage measurements were obtained by monitoring the voltage across the working and SCE reference electrodes while controlling the incident light intensity using a 75 W Xe arc lamp (USHIO UXL 151H, 350 nm – 1350 nm). The flat band potential was extrapolated from the observed saturation (with light intensity) photovoltage.

AC impedance data was collected using an electrochemical cell consisting of the following components: (1) Mg-doped $CuFeO_2$ material as the working electrode; (2) SCE as the reference; (3) a platinium mesh counterelectrode, and (4) 0.1 M $NaHCO_3$ as the electrolyte. Mott-Schottky plots were acquired using a CHI 760D electrochemical workstation operating at 50 kHz and 100 kHz and employing a DC potential range from -0.4 to 0.0 V with a 5 mV peak to peak AC potential perturbation.

Product Detection. Nuclear Magnetic Resonance spectra of post electrolysis solutions were obtained using an automated Bruker Avance-III 500 MHz NMR spectrometer equipped with a C/H –DCH cryoprobe (Bruker-Biospin, Billerica, MA). To enable water suppression, an excitation sculpting method was used.[30] Product concentration was calculated by comparing integrated NMR peaks (MestReNova software) to those of an added known concentration of dioxane as an internal standard.

Linear sweep voltammetry data was collected on either a CHI 760 D or a CHI 1140 A potentiostat. Bulk electrolysis experiments were performed in an H-cell incorporating a salt bridge isolated by glass frits between the electrolysis compartments. Bulk electrolysis was run under potentiostatic conditions (0.05 mA/cm^2 ~ 5 mA/cm^2) for 8 h – 24 h under 470 nm LED (Luxeon V Royal Blue, Future Electronics) illuminated at the surface of the electrode. The p-type $CuFeO_2$ electrode was placed in the same compartment as the SCE reference, with a large area Pt mesh counter electrode (1.5 cm × 1.5 cm) placed in the auxiliary compartment. The headspace of the working compartment was continuously purged with CO_2 or Ar. The pH of the solutions were always maintained at the pH observed under CO_2 bubbling, and were adjusted with 0.1 M HCl under Ar atmosphere.

In a typical photocatalytic experiment, formate was obtained by visible light irradiation (75 W Xe Arc lamp) for 15 h in a sealed pyrex test tube containing 0.3 g of Mg-doped $CuFeO_2$ powder as photocatalyst, 0.1 g $S_2O_3^{2-}$ (or 0.5 g of Zn powder) as the reducing agent, and 10 ml 0.1 M $NaHCO_3$ aqueous solution as the solvent. After photolysis, the powder of Mg-doped $CuFeO_2$(or Zn powder) was filtered by a PTFE(Teflon) Membrane filter (0.2 μm, 17 mm, Sterlitech corporation) and the solution was analyzed by NMR.

Surface Morphology. The morphology and composition of the Mg-doped $CuFeO_2$ was investigated using a Quanta 200 Field Emission Gun Environmental Scanning Electron Microscope (SEM) equipped with an integrated Oxford – Instruments INCA Energy Dispersive X-ray (EDX) system (XMAX 80 square Millimeter detector, detection limit is 0.1% of the excitation volume). Mg concentration cannot be directly determined because it is lower than detection limit of the instrument. Typical EDX results of electrodes before and after electrolysis are provided in Figure S3. X-ray photoelectron spectroscopy (XPS) was performed with a Mg Kα x-ray source (centered at 1253.6 eV) and an electron spectrometer (VG ESCALAB MkII) operated in constant analyzer energy mode with pass energies of 50 and 20 eV for survey and detailed scans, respectively. The photoemission angle was 20 ° with respect to the sample normal, and a base pressure of 10^{-9} torr was maintained throughout the XPS analysis. The C1s peak for aliphatic hydrocarbon at a binding energy of 285.2 eV was used as an internal binding energy reference. [31]

XRD Analysis. To determine compositional changes in the surface layer morphology occurring during electrolysis, powder ray-ray diffraction data were collected and analyzed by Rietveld

refinements[32] with the purpose of microstructural analysis, which was carried out using the FullProf software suite.[33] An alumina standard (NIST 1976a) was used for the analysis. Peak shapes were modeled using the Thompson-Cox-Hastings Pseudo Voight convoluted with Axial Divergence Asymmetry, and particle size broadening was modeled using a symmetry dependent Scherrer analysis.[34] This method uses a spherical harmonic commensurate with the Laue class of the crystal structure.[35,36] Due to the overlapping reflections of Cu and $CuFeO_2$, a two phase refinement was undertaken in which the lattice parameters and the particle size of each phase were refined.

Results and Discussion

Photoresponse Characterization. Chopped illumination**,** photocurrent-potential curve for a Mg-doped $CuFeO_2$ electrode in an aqueous electrolyte containing 0.1M $NaHCO_3$ as the supporting electrolyte but no added CO_2 is shown in Figure 1(A). The dopant level (0.05 %) was chosen based on an effort to maximize photoactivity while retaining conductivity and p-type character. In a preliminary study, we found that higher concentrations of dopant degraded the quality of the semiconductor-electrolyte barrier introducing a large dark current and decreasing the photoactivity of the interface. Lower concentrations decreased the sample conductivity. Samples doped at the 0.05 % - level display p-type character; the resultant photocathodic current increased when scanning towards negative potentials. The observed photocurrent onset potential at -0.1 V *vs.* SCE, was 300 mV more negative than the measured flat band value, *vide infra*. We suspect that the shift in the photocurrent onset potential compared to the measured flat band potential is due to fast charge recombination kinetics under conditions of low band bending as initially suggested by Read.[27]

The incident photon-to-current efficiencies of Mg-doped $CuFeO_2$ electrodes were measured in 0.1 M $NaHCO_3$ solution at -0.4 V *vs*. SCE, where the contribution from dark current is minimal (Figure 1(B)). At the shortest measured wavelength (340 nm), an IPCE efficiency of 14 % was observed. This value dropped significantly moving toward the red, yielding an IPCE of 2 % at 780 nm. The IPCE data for the material reported on here is larger than that reported for thin film $CuFeO_2$ electrodes, by approximately a factor of four.[27] It is likely that the true IPCE increase using the material synthesized here is even greater since we have utilized a relatively thick disk (~1 mm) for the electrode, while the earlier work utilized a thin film sample. In both cases, the resistance of the electrode is uncompensated, and this uncompensated resistance is expected to be larger in the case of the thicker electrode material. Additionally, there is a second uncompensated resistance associated with the back contact to the $CuFeO_2$ sample. We have addressed the latter concern by adjusting the electrode work potential to the electrode-contact material with gold, generating a back contact that is ohmic (see data in Figure 1 inset for a symmetric metal-semiconductor-metal device) having a fairly low impedance. The net sample dc resistance, based on the slope of the plot in the figure is ~60 Ω. This value exaggerates the actual impedance of the device since it is based on a two-probe DC measurement. Ignoring the bulk semiconductor resistance (which is on the order of 1 Ω, based on four point measurements) the $CuFeO_2$/Au junction is generating an uncompensated resistance of <30 Ω.

Band Characterization. The ultraviolet-visible near-infrared (UV-VIS-NIR) absorption spectrum of Mg-doped $CuFeO_2$ is shown in Figure 2(A). The optical band gap (~ 910 nm, 1.36 eV) was found by extrapolating the maximum absorption-edge. The flat band potentials (V_{fb}) of the electrode, essential for elucidating the interfacial solid-liquid energetics of the photoelectrochemical system, were measured by both frequency-dependent Mott-Schottky

measurements and open-circuit photovoltage experiments. The open-circuit potential was measured under various illumination intensities, and it was shown the electrode reached a saturation point or flat band potential at 0.19 V *vs*. SCE electrode in 0.1 M $NaHCO_3$ solution (Figure 2(B)).

Based on the Mott-Schottky equation,

$$\frac{1}{C^2} = \frac{2}{\varepsilon\varepsilon_o A^2 e N_A}\left(V - V_{fb} - \frac{k_B T}{e}\right) \quad (2)$$

(where C is the interfacial capacitance, A is the interfacial area, N_A the number of acceptors, V is the applied voltage, k_B is Boltzmann's constant, T the absolute temperature, and *e* is the electronic charge), a linear plot of C^{-2} *vs* V yields the flat band potential, calculated by subtracting the k_BT/e term from the intersection point on the ordinate. The interfacial capacitance term was found by measuring the bias-dependent impedance of the electrode assuming a simple equivalent circuit model, which accounts for the space charge capacitance at the solid-liquid interface and uncompensated cell resistance. It has been reported by Dutoit *et al*. that a Mott-Schottky plot will yield identical intercept values when modeled by simple equivalent circuits.[37] The Mott-Schottky data shown in Figure 2(C), was obtained at two different frequencies – 50 kHz and 100 kHz. Although a frequency dependent slope is observed, we expect that the data obtained at 100 kHz is in the frequency independent regime (i.e. the time constant for surface state charging should preclude observation of these states at this frequency).[38] Independent of this conclusion, since the ordinate intercept is found to be invariant with frequency an unambiguous value for the flat band potential of +0.2 V *vs*. SCE is obtained. This value is the same, within experimental error, as the value measured using the open-circuit voltage method.

The negative slopes obtained from the Mott-Schottky plot further support our conclusion that the observed photoresponse of this electrode is based on p-type doping.

Assuming that the flat band potential can be taken as a reasonable approximation (i.e. within ~100mV) of the potential of the valence band edge, E_v (0.2 V *vs.* SCE), [39] and subtracting the optical band gap energy from this potential yields the conduction band edge at -1.1 V *vs.* SCE. This is depicted in Figure 2(D), which shows the band edge values of Mg-doped $CuFeO_2$ and the thermodynamic redox potentials of CO_2-reduced products (at the pH employed, 6.8) in a single energy diagram. Appropriate interfacial energetics matching CO_2 reduction energy levels are observed – the conduction band energy of the semiconductor is higher than CO_2-reduction potentials. It is noted, however, that reduction of CO_2 in a simple one electron process to form $CO_2^{-\bullet}$ is not energetically feasible in this system. That is, proton coupled electron transfer (PCET) must be operational for the carbon dioxide reduction to occur in this system.

CO_2 Reduction Capability. To determine electrode activity with CO_2, linear sweep experiments of an illuminated (470 nm, 2.1 mW/cm^2) Mg-doped $CuFeO_2$ electrode in both argon (0.1 M $NaHCO_3$ solution pH adjusted to 6.8) and CO_2 (0.1 M $NaHCO_3$, pH = 6.8) atmospheres were conducted (see Figure 3(A)). Prior work on photoelectrochemical CO_2 reduction hypothesized catalytic mechanisms for reactions of the gas with the semiconductor surface,[8] and thus, a sufficiently slow scan rate of 20 mV/s was utilized to allow for current contribution from any existing redox mechanisms. Figure 3(A) shows strong current enhancement under a CO_2 atmosphere, which is attributed to an interaction between the Mg-doped $CuFeO_2$ surface and CO_2 producing reduced products. It is noted that onset potential differences for linear sweep voltammetry experiments indicate the presence of CO_2 activity as early as -0.2 V *vs.* SCE. At the pH utilized (pH = 6.8) the redox potential for CO_2 reduction to formate (see below) is -0.64 V *vs.*

SCE.[40] Thus, carbon dioxide reduction occurs in the present system at an underpotential of ~400 mV. Though this represents an impressively high underpotential for the reduction of CO_2, in idealized semiconductor systems 300mV of band bending should be sufficient to generate near 100 % charge separation.[41] In the present system this would lead to an onset potential positive of -0.10 V *vs*. SCE, based on the measured flat band potential. The variation in calculated versus observed current onset potential may be attributed to unfavorable kinetics of electron transfer from the photocathode to CO_2. *Nonetheless, the observed onset potential and associated under potential is unprecedented for the direct reduction of CO_2 at an illuminated semiconductor interface.*

To further understand the electrode-CO_2 activity, bulk electrolyses under potentiostatic conditions were performed in CO_2-saturated 0.1 M $NaHCO_3$ under blue LED light illumination (470 nm, 2.1mW/cm^2). These studies were carried out in H-cells, as described in the Experimental section. Electrolysis results using two different electrodes prepared and synthesized using identical conditions are presented in Figure 3(B). Formate, detected by ^{1}H NMR, was the main CO_2-reduced product with a maximum faradaic efficiency of 10 % at -0.9 V *vs*. SCE. Although absolute CO_2 conversion efficiency was not determined using different electrodes, a similar potential-dependence of the conversion efficiency trend was observed. Considerable faradaic loses may be attributed to H_2 production since bubbles were observed on the surface of the electrode. Additionally, $CuFeO_2$ powders are known to catalytically reduce water to H_2 under illumination.[42] Likewise, this electrode will also reduce water at low overpotentials.[27]

Control bulk electrolysis under an Ar atmosphere was performed to determine whether the CO_2-reduced product was derived from a carbon source other than CO_2. Bulk electrolysis at -

0.9 and -1.1 V *vs*. SCE purged with Ar in 0.1 M $NaHCO_3$ did not produce formate, indicating that the product was not derived from $NaHCO_3$. The same electrolyte purged with CO_2, however, produced formate showing that CO_2 is the redox active species. The conversion of $^{13}CO_2$ into $H^{13}COO^-$ was clearly indicated by ^1H NMR spectroscopy after electrolysis for 24 h in a 0.1 M $NaH^{13}CO_3$ solution(Figure S7).This showed the absence of $H^{13}COO^-$ in the pre-electrolysis sample, and the presence of $H^{13}COO^-$ in the post-electrolysis solution.

A control experiment was carried out with Mg-doped $CuFeO_2$ powder.0.3 g of ground Mg-doped $CuFeO_2$ photocatalyst and 0.5 g of Zn powder (or 0.1 g $S_2O_3^{2-}$) were suspended in CO_2 saturated 0.1 M $NaHCO_3$ and illuminated (75 W Xe Arc lamp) for 15 h yielding up to 10^{-4} M formate product. In the photocatalytical system, the photosensitizer Mg-doped $CuFeO_2$ upon excitation, transferring an electron to carbon dioxide, is stable towards photocorrosion by hole consumption reaction utilizing $S_2O_3^{2-}$ or Zn powder as the reducing agents ($E^\circ(Zn^{2+}/Zn)$= - 0.76 V and $E^\circ(S_2O_3^{2-}/SO_3^{2-})$ = -0.57 V). A similar experiment under Ar did not produce any observable formate. These results confirm the favorable thermodynamic energy level alignment of the Mg-doped p-$CuFeO_2$ conduction band with the CO_2 reduction levels.

Surface Morphology. Figure 4 shows the X-ray diffraction (XRD) and scanning electron microscopy (SEM) images for a Mg-doped $CuFeO_2$ electrode surface before and after a 24 h electrolysis under a CO_2 atmosphere. Prior to electrolysis, the SEM image depicts spongiform oxide clusters on the electrode surface, and the XRD pattern matches that found in the ICDD PDF database for $CuFeO_2$. Following electrolysis, the SEM image shows conversion of the spongiform morphology into a more columnar microstructure with ~ 500 nm diameter spherical particles presented on the surface (inset figure).Analysis of the post-electrolysis electrode surface

XRD pattern shows preservation of the delafossite structure. High sensitivity scans of the surface layer, however, reveal a Cu^0 peak in the XRD pattern (expanded in the inset Figure 4). A slight discoloration of the electrode surface after electrolysis, and the observation of no detectable Cu^0 peak when the post-electrolysis electrode is ground into a powder indicate that the Cu^0 exists primarily on the surface of the electrode. Quantitative analysis of the XRD pattern of the electrode after 24 h of electrolysis indicates the formation of Cu^0 with a grain size of ~24 nm on the surface at a level of <0.1% weight fraction of the sample. While only an approximation, this number can be taken as the "surface coverage" of the copper. The XRD data taken after 8 h of electrolysis does not show detectable Cu^0 on the surface (Figure S5), indicating that the formation of Cu^0 is a slow process. At the same time, formate is detected after 8 h of electrolysis (Figure S6), which shows that formate is produced in advance of the generation of Cu^0 on the surface of the electrode. This experiment further confirms Mg-doped $CuFeO_2$ as a catalytic source for the conversion of CO_2." The low Cu^0 content observed by XRD explains why copper particles are not immediately discernible in the SEM images. The particle size of the $CuFeO_2$ estimated from the XRD analysis, 250 nm, is consistent with the SEM images obtained. Elemental analysis of the 24h electrolysis sample by EDX supports the XRD results: an increase in the Cu:Fe ratio from 1 : 1 to 1.3 : 1 (supporting information Figure S3) is observed. Similarly, XPS analysis (Figure S4) only yields a Cu^I peak for the $CuFeO_2$ electrode surface prior to electrolysis. After a 24 h electrolysis, however, a Cu^0 peak is detected. [43,44] Although Cu metal is a known electrocatalyst for CO_2 reduction,[45] the low quantity of Cu^0 and high quantity of formate observed in these experiments rules out Cu^0 as the catalytic source of CO_2 reduction in the present system.

Conclusion

Photoelectrochemical reduction of CO_2 to fuel would enable a sustainable method to recycle this greenhouse gas. However, to reach this goal new small band gap semiconductor materials that are affordable and accessible are required. In this work, a p-type Mg-doped $CuFeO_2$ electrode, made from readily available compounds and prepared by a straightforward solid-state method, has been found to photoelectrochemically reduce CO_2 to formate unparalleled underpotential without need for a cocatalyst. However, the main competition process in this photoelectrochemical process is the reduction of water into H_2.

The observation that suspended Mg-doped $CuFeO_2$ powders are capable of converting CO_2 to formate under illumination suggests optimization of this or related oxide based system could lead to a stable and efficient solar fuel reactor for the conversion of CO_2 to organic products without application of an external bias. Further study of this delafossite system, however, must include techniques to stabilize this and similar materials against slow degradation via the formation of reduced products such as the Cu^0 observed in the present study. To this end, the methodological integration of solid-state synthesis with electrochemical analysis provides an avenue to identify and optimize new materials as semiconductor photoelectrodes.

FIGURES

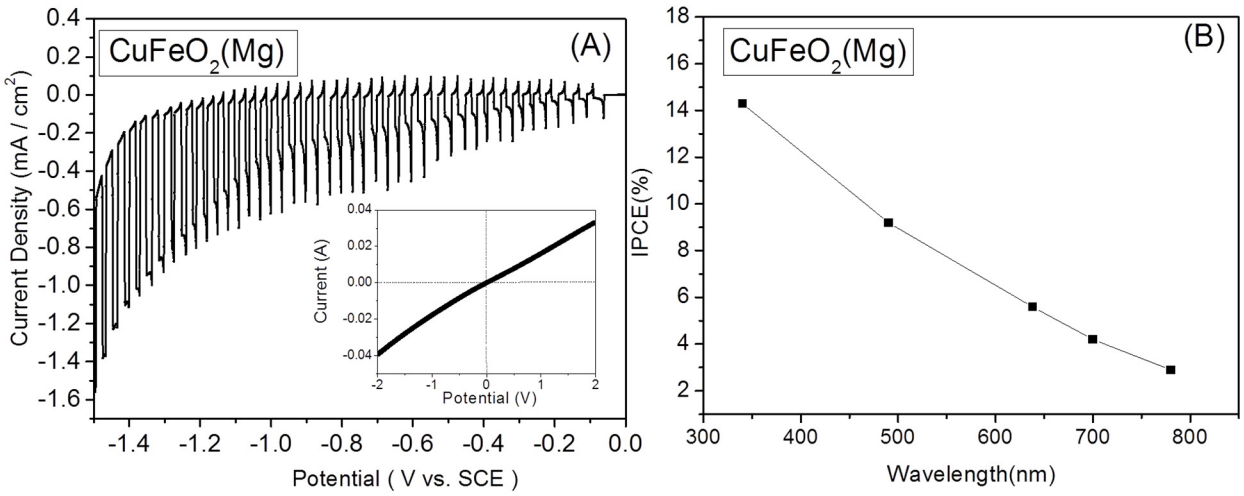

Figure 1. (A) Linear sweep voltammetry of Mg-doped $CuFeO_2$ using chopped light in 0.1 M $NaHCO_3$ yields a photocurrent density up to -1.0 mA/cm^2 (Scan rate 100 mV/s), inset: The near linear current-voltage curve, obtained by performing a linear sweep experiment on an electrode with Au sputtered on both faces and connected to working, counter and reference leads by a copper wire, indicates the formation of an ohmic contact. (B) The Incident Photon to Current Efficiency (IPCE %) obtained at -0.4 V *vs.* SCE in 0.1 M $NaHCO_3$ in air, and measured from 780 nm to 340 nm.

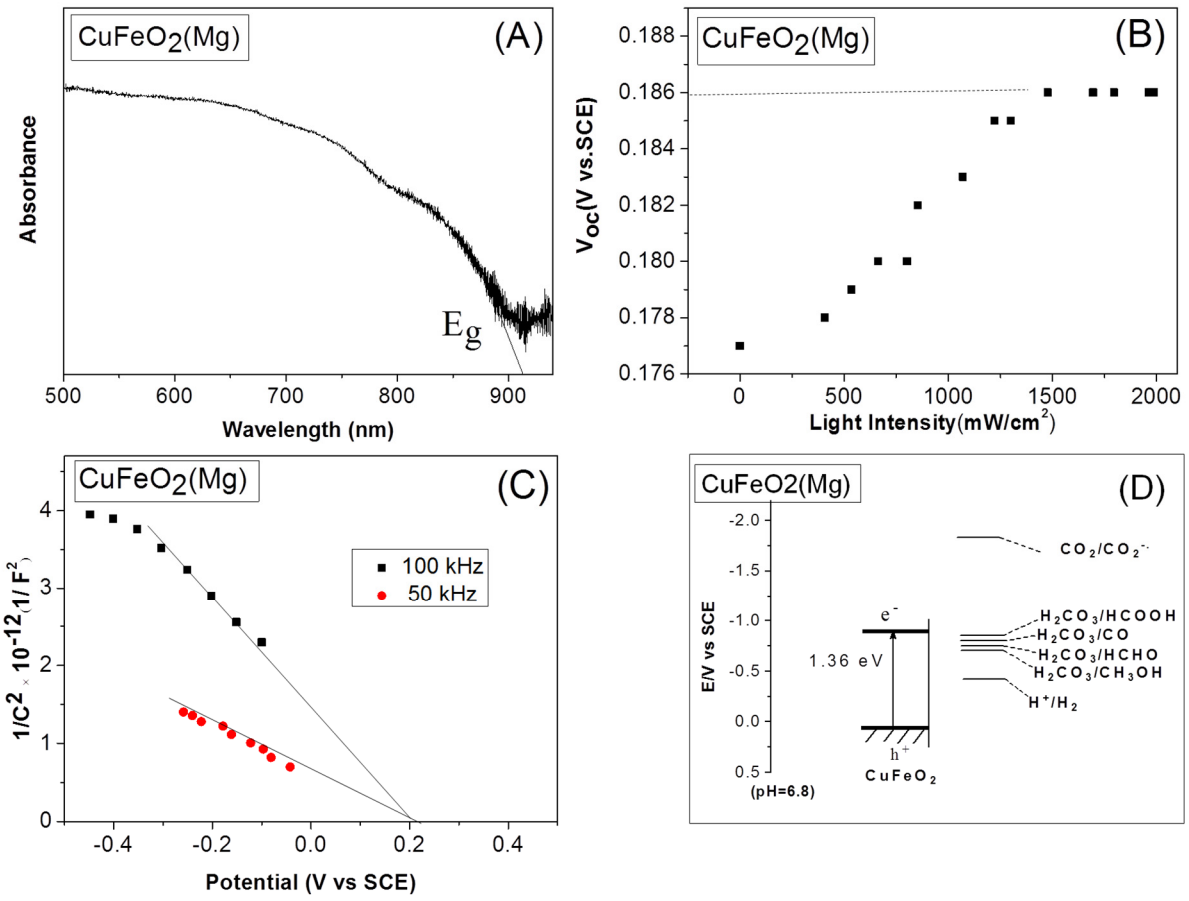

Figure 2. (A) Extrapolation of the absorbance edge given by the UV-Vis-NIR absorption spectrum of Mg-doped $CuFeO_2$ yields an optical band gap of 1.36 eV. (B) Open circuit photovoltage measurement, performed in a two-electrode cell with Mg-doped $CuFeO_2$ as the working electrode and SCE as the reference electrode, shows saturation at 0.19 V *vs*. SCE in 0.1 $NaHCO_3$ solution, attributed to the flat band potential of the semiconductor electrode. (C) Mott-Schottky plots collected at frequencies 50 kHz (red) and 100 kHz (black) of the Mg-doped $CuFeO_2$ electrode in 0.1 M $NaHCO_3$ solution were measured in the dark. The x-intercept yields the flat band potential, 0.2 V *vs*. SCE. (D) Experimentally determined Mg-doped $CuFeO_2$ conduction and valence band edges and thermodynamic redox potentials of CO_2 reduction products on a potential diagram, depicting favorable energetics for photo-assisted CO_2 reduction.

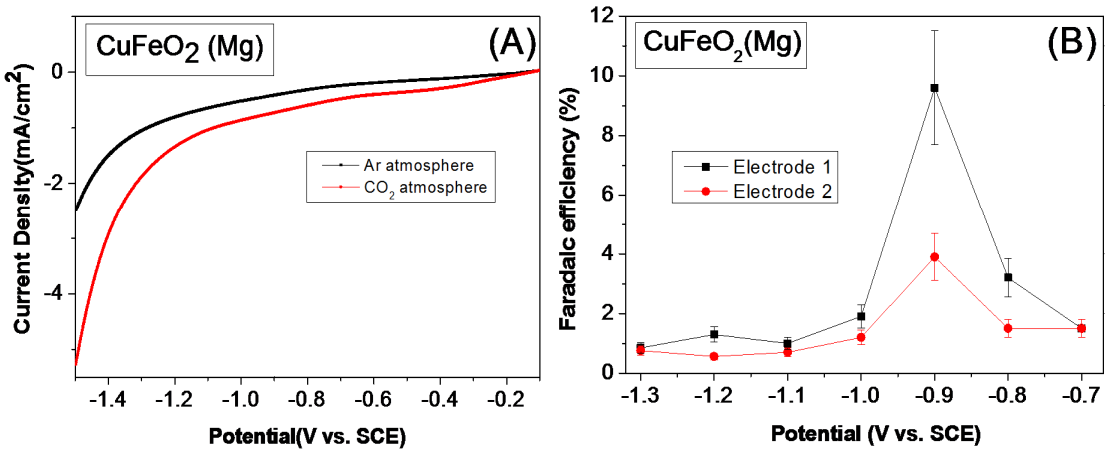

Figure 3. (A) Current-Potential curves obtained for 470 nm LED illuminated Mg-doped $CuFeO_2$ electrode in 0.1 M $NaHCO_3$ under Ar atmosphere adjusted to pH 6.8 (black line) and in 0.1 M $NaHCO_3$ saturated with CO_2 at pH 6.8 (red line) (B) Faradaic efficiency for formate vs. potential shows maximum conversion efficiency at -0.9 V *vs*. SCE and similar trends for electrodes prepared using identical synthesis and prepared conditions.

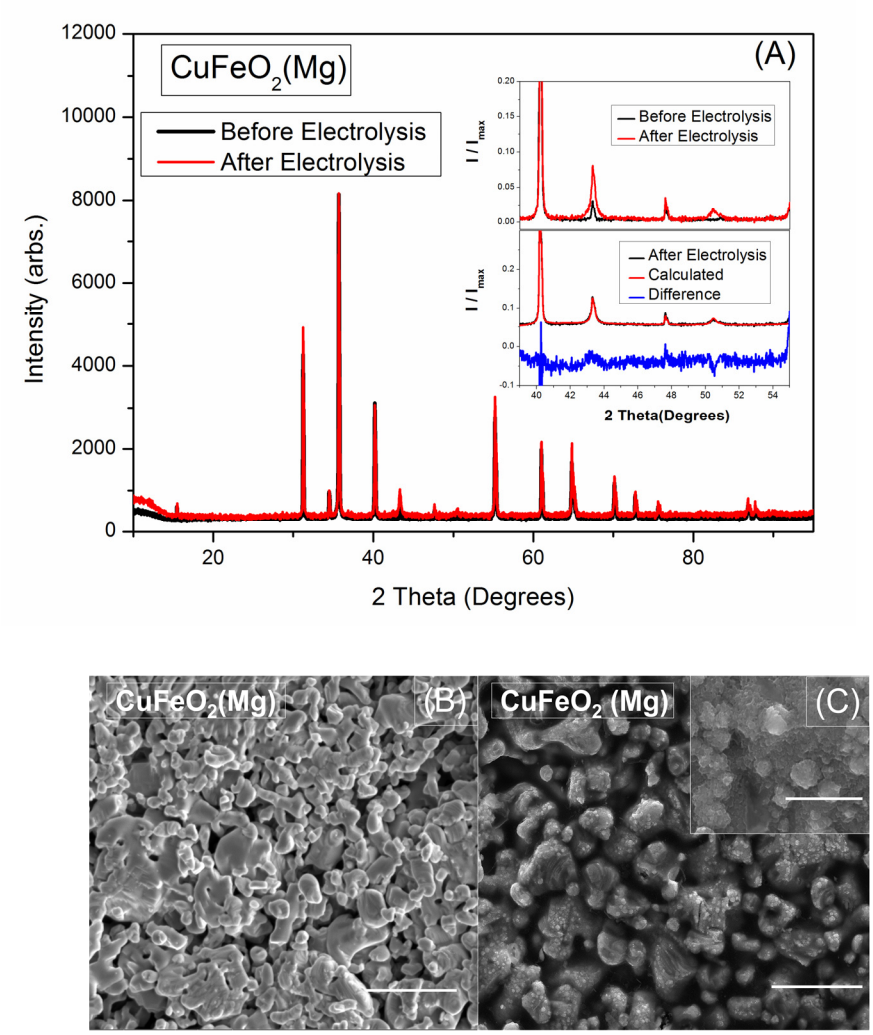

Figure 4. (A) XRD of a polycrystalline Mg-doped $CuFeO_2$ electrode before electrolysis (black) and after electrolysis (red). The post-electrolysis pattern (see inset) indicates formation of elemental copper on the electrode surface. Inset: Rietveld refinement of post-electrolysis photoelectrode (bottom) and pre-electrolysis XRD pattern compared with post-electrolysis XRD pattern (top). (B) SEM image of Mg-doped $CuFeO_2$ pellet sintered under Ar atmosphere for 12h prior to electrolysis, scale bar : 10 μm. (C) SEM image of the same electrode after electrolysis at -1.0 V *vs*. SCE in 0.1 M $NaHCO_3$ for 24 h in a CO_2 atmosphere, scale bar : 10 μm, inset figure scale bar: 1 μm.

ASSOCIATED CONTENT

Supporting Information. Detailed of calculations related to the IPCE measurements, characterization analyses from EDX and XPS spectra, and XRD patterns of the Mg-doped $CuFeO_2$ pellet surface after 8 h electrolysis are provided in the supplemental information. This material is available free of charge via the internet at http://pubs.acs.org.

Corresponding Author

*Email: bocarsly@princeton.edu. Tel.: 609-258-3888.

Author Contributions

The manuscript was written through contributions of all authors. All authors have given approval to the final version of the manuscript.

ACKNOWLEDGEMENT

The authors acknowledge support of this research from the Office of Basic Energy Sciences, Department of Energy. The solid-state synthesis and physical characterization of materials were carried out under the direction of RJC under grant DE-FG02-98ER45706. Photoelectrochemical experiments and analysis were carried out under the direction of ABB under grant DE-SC0002133. The authors also acknowledge Mr. Fei Ding and Professor S. Y. Chou in the Electrical Engineering Department of Princeton University for assisting in the Au sputtering procedures and semiconductor absorbance experiments.

REFERENCES

(1) Morris, A. J.; Meyer, G. J.; Fujita, E. Molecular approaches to the photocatalytic reduction of carbon dioxide for solar fuels. *Accounts. Chem. Res.* **2009**, *42*, 1983-1994.

(2) Fujita, E.: Photochemical carbon dioxide reduction with metal complexes. *Coord. Chem. Rev.* **1999**, *185*, 373-384.

(3) Takeda, H.; Ishitani, O.: Development of efficient photocatalytic systems for CO_2 reduction using mononuclear and multinuclear metal complexes based on mechanistic studies. *Coord. Chem. Rev.* **2010**, *254*, 346-354.

(4) Liang, Y. T.; Vijayan, B. K.; Gray, K. A.; Hersam, M. C.: Minimizing Graphene Defects Enhances Titania Nanocomposite-Based Photocatalytic Reduction of CO2 for Improved Solar Fuel Production. *Nano lett.* **2011**, *11*, 2865-2870.

(5) Tsai, C. W.; Chen, H. M.; Liu, R. S.; Asakura, K.; Chan, T. S.: Ni@ NiO Core–Shell Structure-Modified Nitrogen-Doped InTaO4 for Solar-Driven Highly Efficient CO_2 Reduction to Methanol. *J. Phys. Chem. C* **2011**, *115*, 10180-10186.

(6) Izumi, Y.: Recent advances in the photocatalytic conversion of carbon dioxide to fuels with water and/or hydrogen using solar energy and beyond. *Coordin. Chem. Rev.* **2013**, *257*, 171-186.

(7) Aurian-Blajeni, B.; Halmann, M.; Manassen, J.: Electrochemical measurement on the photoelectrochemical reduction of aqueous carbon dioxide on p-Gallium phosphide and p-Gallium arsenide semiconductor electrodes. *Sol. Energy Mater.* **1983**, *8*, 425-440.

(8) Barton, E. E.; Rampulla, D. M.; Bocarsly, A. B.: Selective solar-driven reduction of CO_2 to methanol using a catalyzed p-GaP based photoelectrochemical cell. *J. Am. Chem. Soc.* **2008**, *130*, 6342-6344.

(9) Halmann, M.: Photoelectrochemical reduction of aqueous carbon dioxide on p-type gallium phosphide in liquid junction solar cells. *Nature* **1978**, *275*, 115.

(10) Kaneco, S.; Katsumata, H.; Suzuki, T.; Ohta, K.: Photoelectrochemical reduction of carbon dioxide at p-type gallium arsenide and p-type indium phosphide electrodes in methanol. *Chem. Eng. J.* **2006**, *116*, 227-231.

(11) Preusser, S.; Herlem, M.; Etcheberry, A.; Jaume, J.: The photodissolution of InP. *Electrochim. Acta.* **1992**, *37*, 289-295.

(12) Ida, S.; Yamada, K.; Matsunaga, T.; Hagiwara, H.; Matsumoto, Y.; Ishihara, T.: Preparation of p-Type $CaFe_2O_4$ Photocathodes for Producing Hydrogen from Water. *J. Am. Chem. Soc.* **2010**, *132*, 17343-17345.

(13) Tilley, S. D.; Cornuz, M.; Sivula, K.; Grätzel, M.: Light-Induced Water Splitting with Hematite: Improved Nanostructure and Iridium Oxide Catalysis. *Angew. Chem. Int. Edit.* **2010**, *122*, 6549-6552.

(14) Higashi, M.; Domen, K.; Abe, R.: Highly Stable Water Splitting on Oxynitride TaON Photoanode System under Visible Light Irradiation. *J. Am. Chem. Soc.* **2012**, *134*, 6968-6971.

(15) Bocarsly, A. B.; Gibson, Q. D.; Morris, A. J.; L'Esperance, R. P.; Detweiler, Z. M.; Lakkaraju, P. S.; Zeitler, E. L.; Shaw, T. W.: Comparative Study of Imidazole and Pyridine Catalyzed Reduction of Carbon Dioxide at Illuminated Iron Pyrite Electrodes. *ACS Catal.***2012**, *2*, 1684-1692.

(16) Yoneyama, H.; Sugimura, K.; Kuwabata, S.: Effects of electrolytes on the photoelectrochemical reduction of carbon dioxide at illuminated p-type cadmium telluride and p-type indium phosphide electrodes in aqueous solutions. *J. Electroanal. Chem. Interfac. Electrochem.* **1988**, *249*, 143-153.

(17) Bradley, M. G.; Tysak, T.; Graves, D. J.; Viachiopoulos, N. A.: Electrocatalytic reduction of carbon dioxide at illuminated p-type silicon semiconduccting electrodes. *J. Chem. Soc., Chem. Commun.* **1983**, 349-350.

(18) Matsumoto, Y.; Obata, M.; Hombo, J.: Photocatalytic reduction of carbon dioxide on p-type $CaFe_2O_4$ powder. *J. Phys. Chem.* **1994**, *98*, 2950-2951.

(19) Galakhov, V.; Poteryaev, A.; Kurmaev, E.; Anisimov, V.; Neumann, M.; Lu, Z.; Klein, B.; Zhao, T. R.: Valence-band spectra and electronic structure of $CuFeO_2$. *Phys. Rev. B* **1997**, *56*, 4584.

(20) Thurston, T.; Wilcoxon, J.: Photooxidation of organic chemicals catalyzed by nanoscale MoS2. *J. Phys. Chem. B* **1999**, *103*, 11-17.

(21) Marquardt, M. A.; Ashmore, N. A.; Cann, D. P.: Crystal chemistry and electrical properties of the delafossite structure. *Thin Solid Films* **2006**, *496*, 146-156.

(22) Mugnier, E.; Barnabé, A.; Tailhades, P.: Synthesis and characterization of $CuFeO_2^{2+}$ delafossite powders. *Solid State Ionics* **2006**, *177*, 607-612.

(23) Scanlon, D. O.; Watson, G. W.: Understanding the p-type defect chemistry of $CuCrO_2$. *J. Mater. Chem.* **2011**, *21*, 3655-3663.

(24) Benko, F. A.; Koffyberg, F. P.: Opto-Electronic Properties of p- and n-Type Delafossite $CuFeO_2$. *J. Phys. Chem. Solids* **1986**, *48*, 431-434.

(25) Omeiri, S.; Bellal, B.; Bouguelia, A.; Bessekhouad, Y.; Trari, M.: Electrochemical and photoelectrochemical characterization of $CuFeO_2$ single crystal. *J. Solid. State. Electrochem.* **2009**, *13*, 1395-1401.

(26) Omeiri, S.; Gabes, A.; Bouguelia, A.; Trari, M.: Photoelectrochemical characterization of the delafossite $CuFeO_2$: Applications to removal of divalent metal ions. *J. Electroanal. Chem.* **2008**, *614*, 31-40.

(27) Read, C. G.; Park, Y.; Choi, K.-S.: Electrochemical Synthesis of p-Type $CuFeO_2$ Electrodes for Use in a Photoelectrochemical Cell. *J. Phys. Chem. Lett.* **2012**, *3*, 1872-1876.

(28) Pabst, A.: Crystal Structure and Density of Delafossite. *American Mineralogist* **1938**, *23*, 175-176.

(29) Sell, D.: Resolved free-exciton transitions in the optical-absorption spectrum of GaAs. *Phys. Rev. B* **1972**, *6*, 3750.

(30) Hwang, T. L.; Shaka, A.: Water suppression that works. Excitation sculpting using arbitrary wave-forms and pulsed-field gradients. *J. Magn. Reson. A* **1995**, *112*, 275-279.

(31) Wallart, X.; Henry de Villeneuve, C.; Allongue, P.: Truly Quantitative XPS Characterization of Organic Monolayers on Silicon: Study of Alkyl and Alkoxy Monolayers on H−Si(111). *J. Am. Chem. Soc.* **2005**, *127*, 7871-7878.

(32) Rietveld, H.: A profile refinement method for nuclear and magnetic structures. *J. Appl. Crystallogr.* **1969**, *2*, 65-71.

(33) Rodríguez-Carvajal, J.: Recent advances in magnetic structure determination by neutron powder diffraction. *Physica. B.: Condens. Matter.* **1993**, *192*, 55-69.

(34) Scherrer, P.: Bestimmung der Grösse und der inneren Struktur von Kolloidteilchen mittels Röntgenstrahlen. *Gott. Nachr.* **1918**, *1918*, 98-100.

(35) Popa, N.: The (hkl) dependence of diffraction-line broadening caused by strain and size for all Laue groups in Rietveld refinement. *J. Appl. Crystallogr.* **1998**, *31*, 176-180.

(36) Popa, N.; Balzar, D.: Size-broadening anisotropy in whole powder pattern fitting. Application to zinc oxide and interpretation of the apparent crystallites in terms of physical models. *J. Appl. Crystallogr.* **2008**, *41*, 615-627.

(37) Dutoit, E. C. V. M., R.L.; Cardon, F. : *Ber. Bunsenges. Phys. Chem.* **1975**, *79*, 1206.

(38) Morrison, S. R.: *Electrochemistry at Semiconductors and Oxidized Metal Electrodes* **1980**, *Plenum Press, New York*

(39) Finklea, H. O.: *Semiconductor electrodes*; Elsevier, 1988.

(40) Reda, T.; Plugge, C. M.; Abram, N. J.; Hirst, J.: Reversible interconversion of carbon dioxide and formate by an electroactive enzyme. *Proc. Natl. Acad. Sci.* **2008**, *105*, 10654-10658.

(41) Bocarsly, A. B.; Hiroyasu, H.; Faulkner, L. R.: Photonic Electrochemistry. In *Laboratory Techniques in Electroanalytical Chemistry*; 2nd ed.; Kissinger, P. T., Heineman, W. R., Eds.; Marcel Dekker: New York, 1996; pp 855-900.

(42) Derbal, A.; Omeiri, S.; Bouguelia, A.; Trari, M.: Characterization of new heterosystem $CuFeO_2/SnO_2$ application to visible-light induced hydrogen evolution. *Int. J. Hyrogen. Energ.* **2008**, *33*, 4274-4282.

(43) Le, M.; Ren, M.; Zhang, Z.; Sprunger, P.; Kurtz, R.; Flake, J.: Electrochemical Reduction of CO_2 to CH_3OH at Copper Oxide Surfaces. *J. Electrochem. Soc.* **2011**, *158*, E45-E49.

(44) Hirsimäki, M.; Lampimäki, M.; Lahtonen, K.; Chorkendorff, I.; Valden, M.: Investigation of the role of oxygen induced segregation of Cu during Cu_2O formation on Cu {100}, Ag/Cu {100} and Cu (Ag) alloy. *Surf. Sci.* **2005**, *583*, 157-165.

(45) Hori, Y.: Electrochemical CO 2 reduction on metal electrodes. *Mod. Aspect. Electroc.* **2008**, 89-189.

Table of contents